Supplementary Information

1. Material Characterization

1.1 Structural analysis

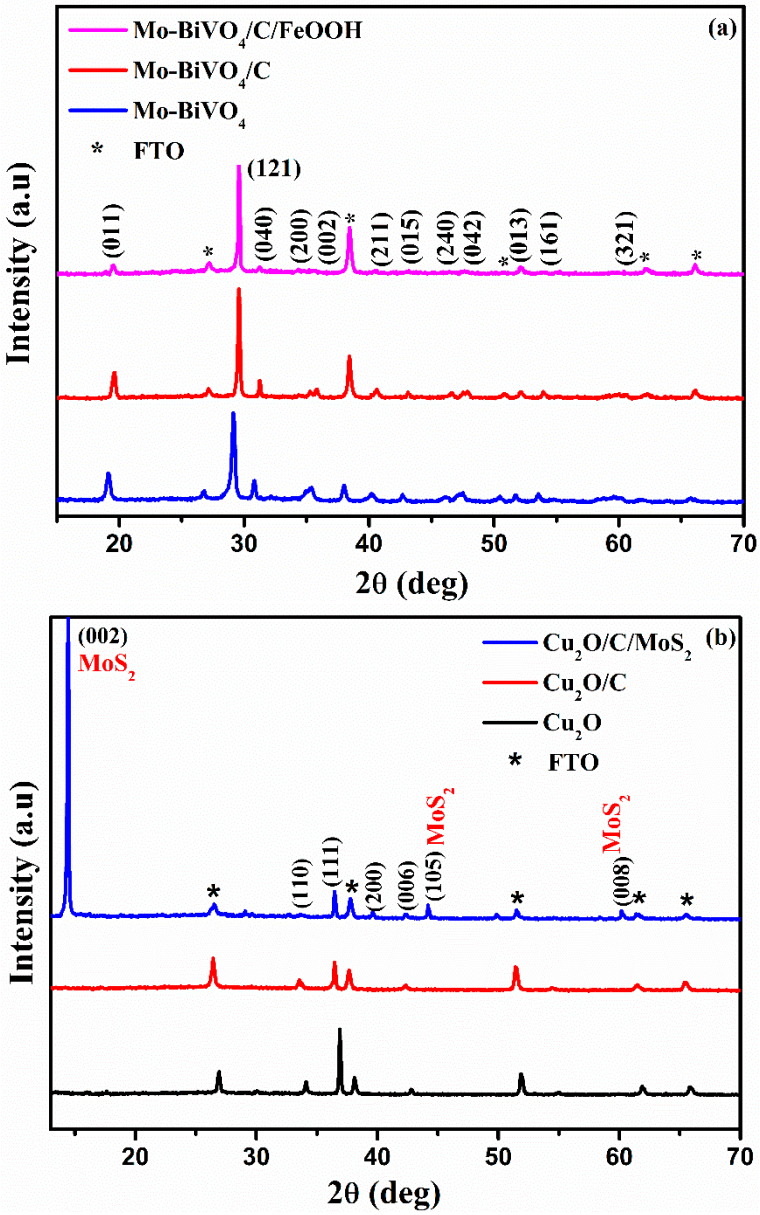

Figure S1, *(a) XRD spectra of Mo-BiVO4, Mo-BiVO4/C and Mo-BiVO4/C/FeOOH photoanode and (b) Cu2O, Cu2O/C and Cu2O/C/MoS2 photocathodes*

Crystallinity of the as-prepared $BiVO_4$ photoanodes was analysed using XRD and the spectra are presented in figure S1. It is important that desired crystallinity should be formed in photoanode/photocathode which leads to better performance in tandem cell. From the XRD spectra, the diffraction peaks of all the photoanodes contain signature peaks at 28.9° for $BiVO_4$. All the diffraction peaks are well indexed with JCPDS card no. 14-0688 [27]. The lattice constants are a = 5.1950 Å, b = 11.7010 Å and c = 5.0920 Å. Tetragonal phase of $BiVO_4$ formed due to the intermediate annealing during the synthesis process. At the final annealing stage, the phase changed completely to monoclinic scheelite phase of $BiVO_4$ [28]. Monoclinic scheelite $BiVO_4$ is suitable for photocatalytic applications [29]. The shift in the signature peak from

28.9° to 29.1° determines the presence of molybdenum dopant in place of some vanadium lattice points as a result of the compressive strain induced in monoclinic scheelite $BiVO_4$. No extra diffraction peaks were found for carbon and FeOOH in the photoanodes due to their low content.

Crystalline information of Cu_2O photocathodes is presented in figure S1 (b). The obtained diffraction spectrum of all photocathodes contain the signature peaks of Cu_2O at 36.8° and 43.44°. The diffraction peaks of Cu_2O photocathodes corresponds to the JCPDS card no. 65-3288 [30]. The lattice constants are a = b = c = 4.2520 Å. The entire as-deposited Cu_2O photocathode was cubic structure. No impurities such as copper oxide (CuO) or copper are found in the XRD spectra. The crystal structure of $BiVO_4$ and Cu_2O is monoclinic scheelite and cubic structures, respectively. For tandem PEC cell, Cu_2O/C photocathode was loaded with MoS_2 and termed as Cu_2O/C/MoS_2. Addition of HER catalyst MoS_2 was confirmed with the signature peak at 14.4° for MoS_2 [31]. XRD spectra of Cu_2O/C/MoS_2 photocathodes corresponds to diffraction spectra of cubic Cu_2O and MoS_2.

Raman Vibrational analysis

Table S1, *Tabulation of significance of $BiVO_4$ photoanodes*

Peaks (cm^{-1})	***Significance***
209.15	External mode of monoclinic $BiVO_4$
327.28 and 363.87	Symmetric and asymmetric deformation of VO_4^{3-}
823.83	Symmetric stretch mode of V – O
877.09	Stretching of O – Mo – O
1330.54	I_D band of carbon
1588.09	I_G band of carbon

Table S2, *Tabulation of significance of Cu_2O photocathodes*

Peak (cm^{-1})	***Significance***
213.39	Second order raman mode of Cu_2O
626.39	Infrared allowed mode of Cu_2O

375.92	In-plane mode of vibration of MoS_2
403.44	Out-plane mode of vibration of MoS_2
1333.70	I_D band of carbon
1569.65	I_G band of carbon

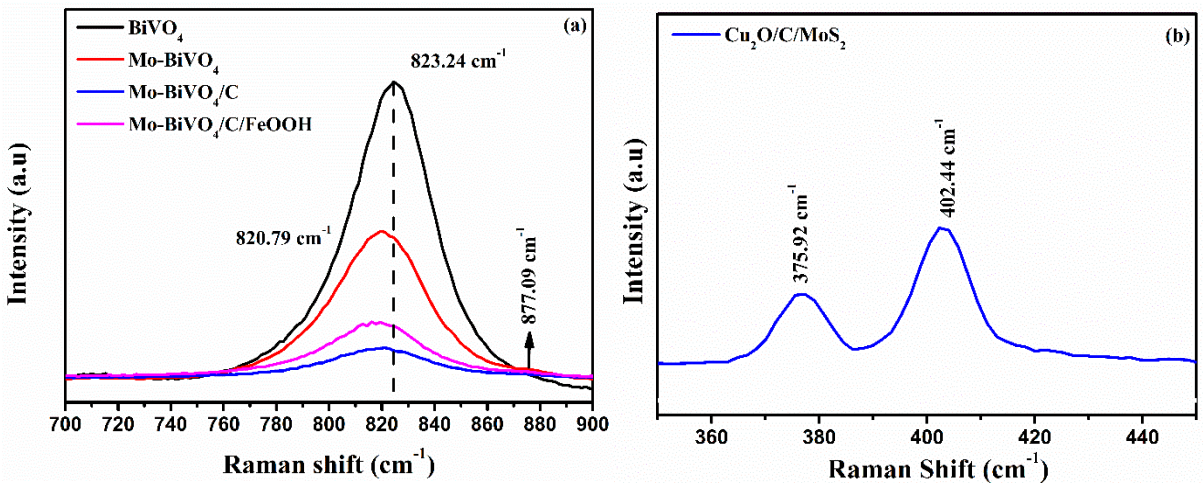

Figure S2, *(a) Zoomed Raman Spectra of $BiVO_4$ photoanodes which presents the blue shift in the peak at 823.24 $cm^{-1}$to 820.79 cm^{-1} due to doping of Molybdenum (b) Zoomed Raman Spectra of $Cu_2O/C/MoS_2$ photocathode which confirms the presence of MoS_2 on $Cu_2O/C/MoS_2$ photocathode*

1.2 Morphological analysis

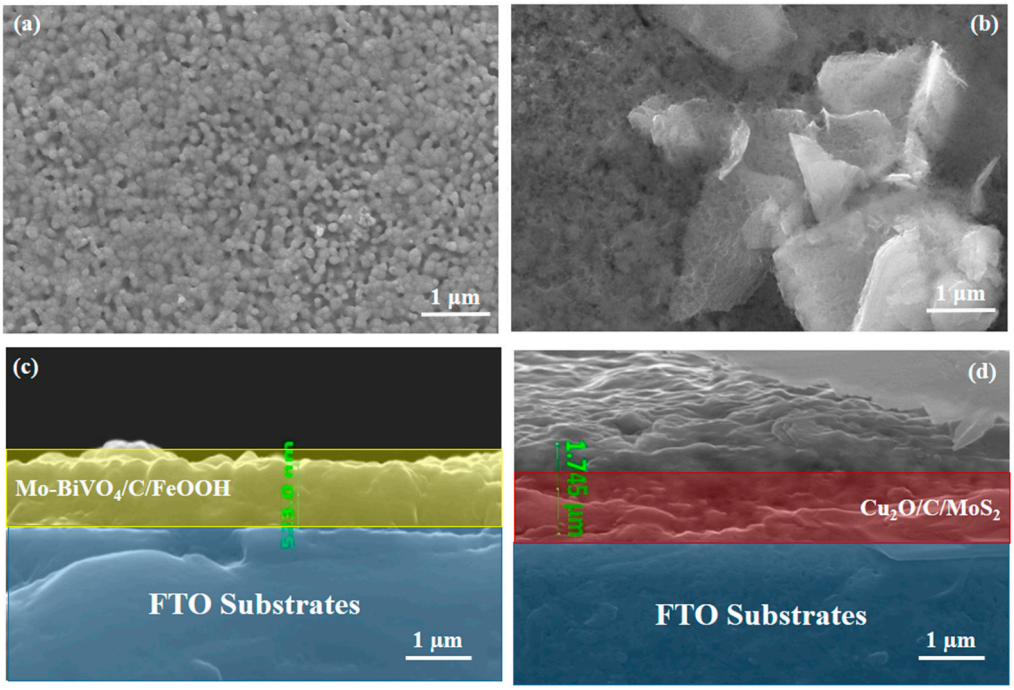

Figure S3, *FESEM micrograph of (a) Mo-BiVO4/C/FeOOH photoanode, (b) Cu2O/C/MoS2 photocathode and Cross sectional FESEM micrograph of (c) Mo-BiVO$_4$/TiO$_2$/FeOOH photoanode and (d) Cu$_2$O/TiO$_2$/MoS$_2$ photocathode*

From figure S3 (a), the conformal coating of FeOOH was also observed throughout the photoanodes as a translucent coating. Similarly, the deposition of MoS_2 was confirmed through a sheet-like coating throughout the Cu_2O/C surface from figure S3 (b).

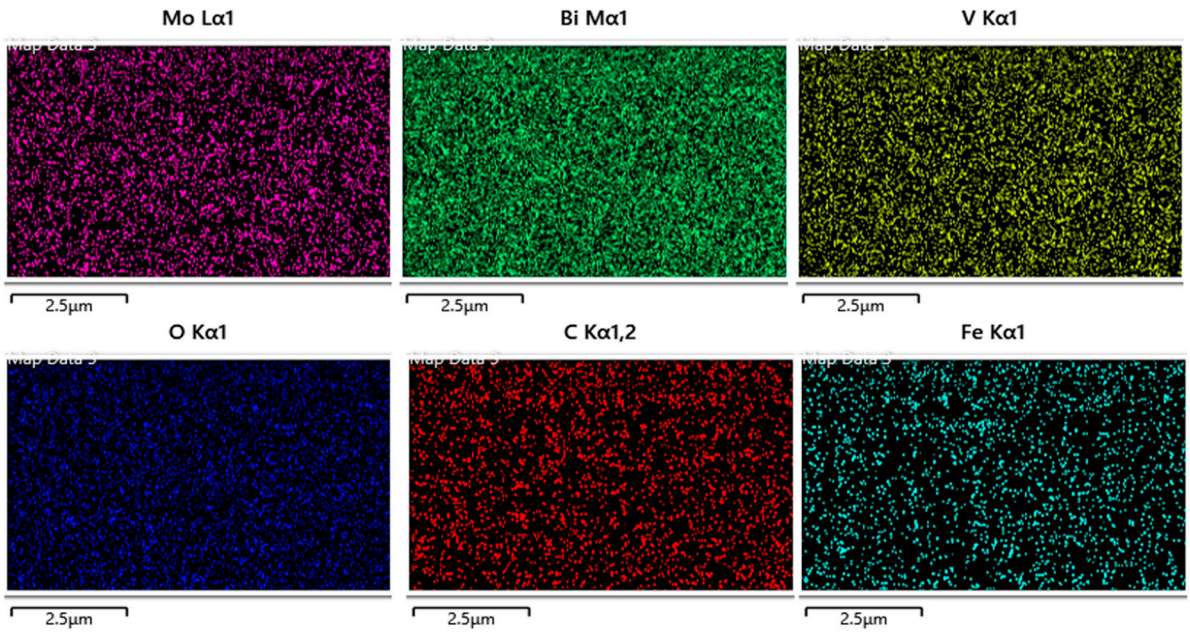

Figure S4, *EDS colour mapping of Mo-BiVO$_4$/C/FeOOH photoanode*

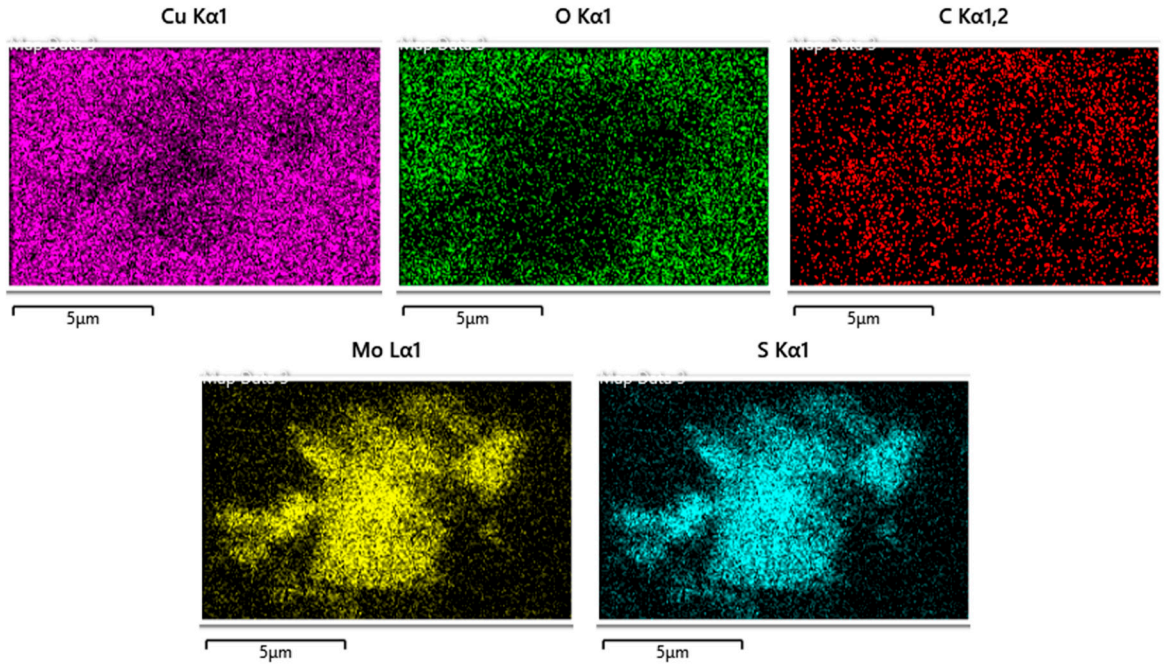

Figure S5, *EDS colour mapping of $Cu_2O/C/MoS_2$ photocathode*

1.3 Optical analysis

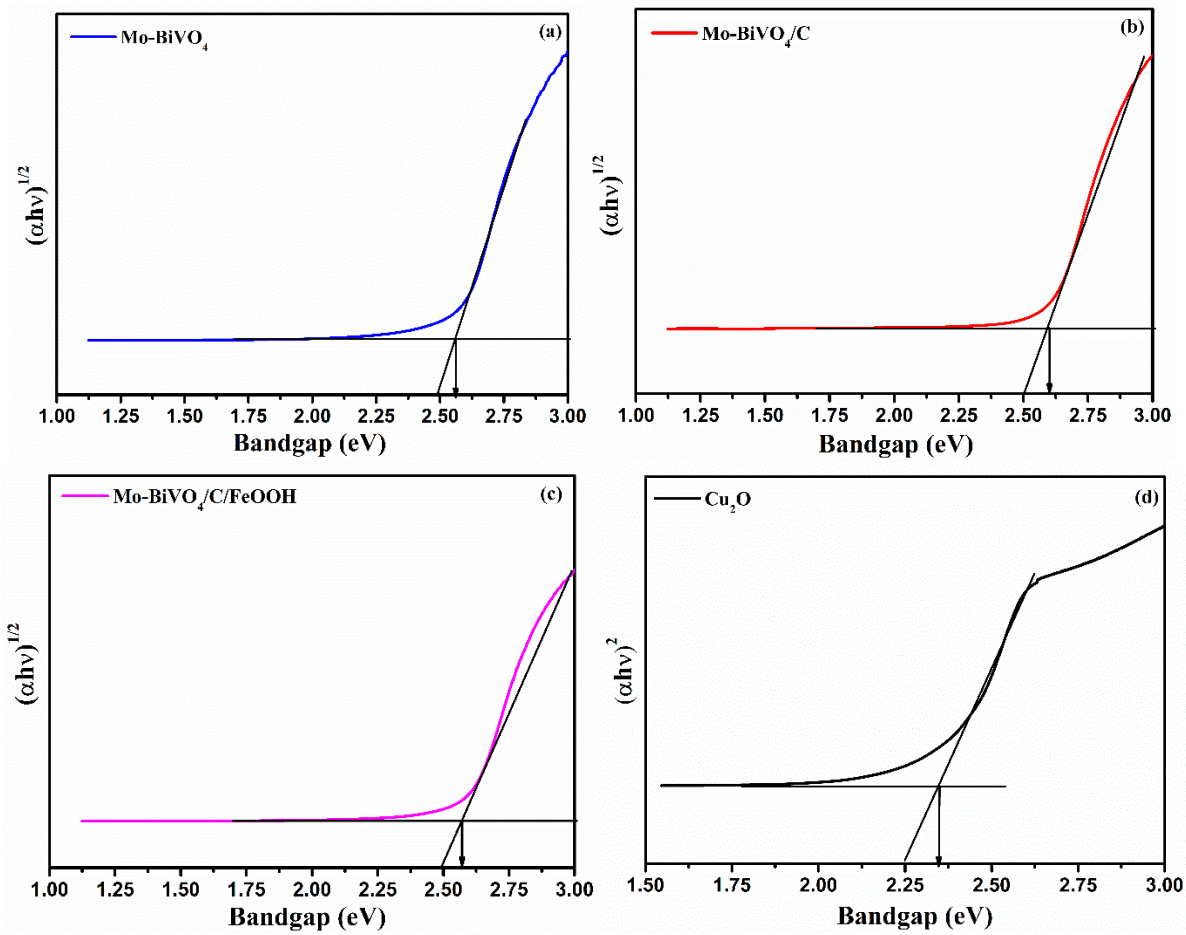

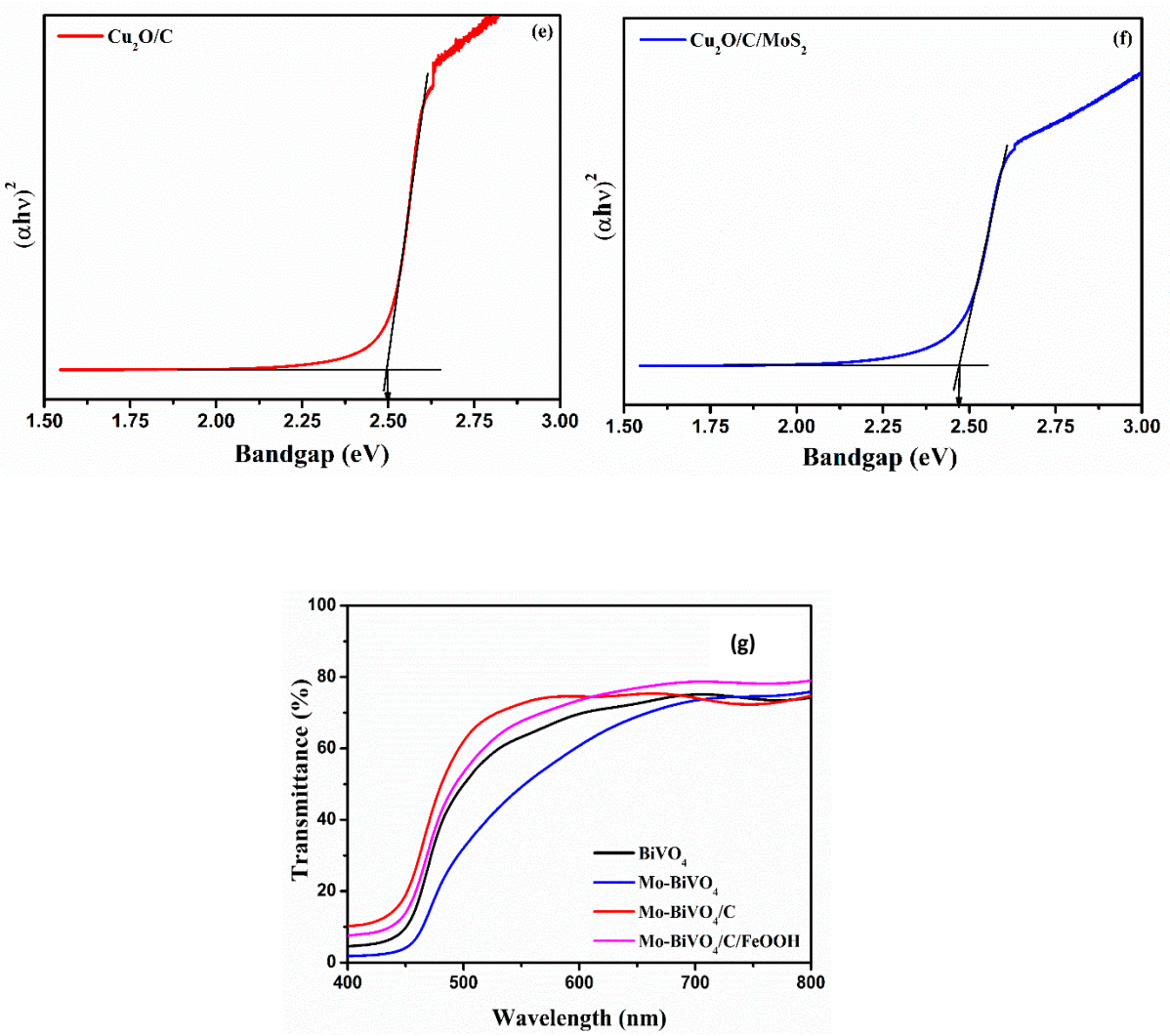

Figure S6, *Tauc Plot extrapolation of (a) Mo-$BiVO_4$, (b) Mo-$BiVO_4$/C, (c) Mo-$BiVO_4$/C/FeOOH photoanodes and (d) Cu_2O, (e) Cu_2O/C and (f) Cu_2O/C/MoS_2 photocathodes (g) Transmittance of $BiVO_4$, Mo-$BiVO_4$, Mo-$BiVO_4$/C, Mo-$BiVO_4$/C/FeOOH photoanodes*

1.4 Photoluminescence studies

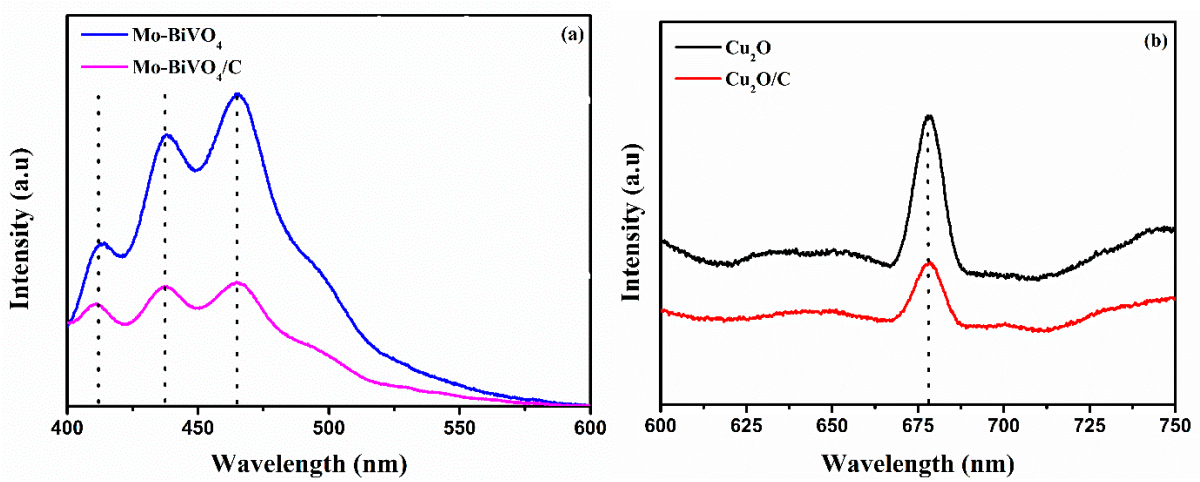

Figure S7, *Photoluminescence spectra of (a) Mo-BiVO4, Mo-BiVO4/C photoanodes and (b) Cu2O, Cu2O/C photocathodes*

Photoluminescence studies were performed on Mo-$BiVO_4$, Mo-$BiVO_4$/C photoanodes and Cu_2O, Cu_2O/C photocathodes to understand the charge carrier dynamics in the photoelectrodes. The radiative recombination of photoinduced electron-hole pair can be investigated using PL spectra shown in figure S7. In PL spectra, low PL intensity means lower photogenerated electron-hole recombination which corresponds to efficient charge carrier separation. Figure S7 (a) shows the PL spectra of Mo-$BiVO_4$ and Mo-$BiVO_4$/C photoanodes. The excitation wavelength used for Mo-$BiVO_4$ photoanodes was 350 nm. Figure S7 (a) shows multiple radiative emission peaks due to doping of Mo. In the figure, Mo-$BiVO_4$ photoanode exhibits higher PL intensity which implies that recombination is high in the photoanode but the intensity Mo-$BiVO_4$/C is greatly reduced. The reduced PL intensity is ascribed to the low recombination and also higher charge carrier separation due to the addition of carbon layer. The decrease in the PL intensity implies photoluminescence quenching and better charge transfer between carbon layer and Mo-$BiVO_4$ [32] [33] [34]. Similarly, PL spectra of Cu_2O and Cu_2O/C photocathodes were shown in figure S7 (b). PL spectra was measured using an excitation wavelength of 450 nm. The PL peaks of both photocathodes was around 670 nm. The peak confirms the emission of Cu_2O. The intensity of Cu_2O/C was quenched than bare Cu_2O which means that carbon coated Cu_2O provides better charge transfer than bare Cu_2O photocathode. The result indicates that carbon layer facilitates effective separation and transportation of charge carriers [35] [36]. The quenching of PL intensity in both Mo-$BiVO_4$ photoanodes and Cu_2O photocathodes by carbon layer could increase the PEC performance when they are employed in tandem cell.

2. *Photoelectrochemical analysis*

2.1 *Stability tests of photoanodes and photocathodes*

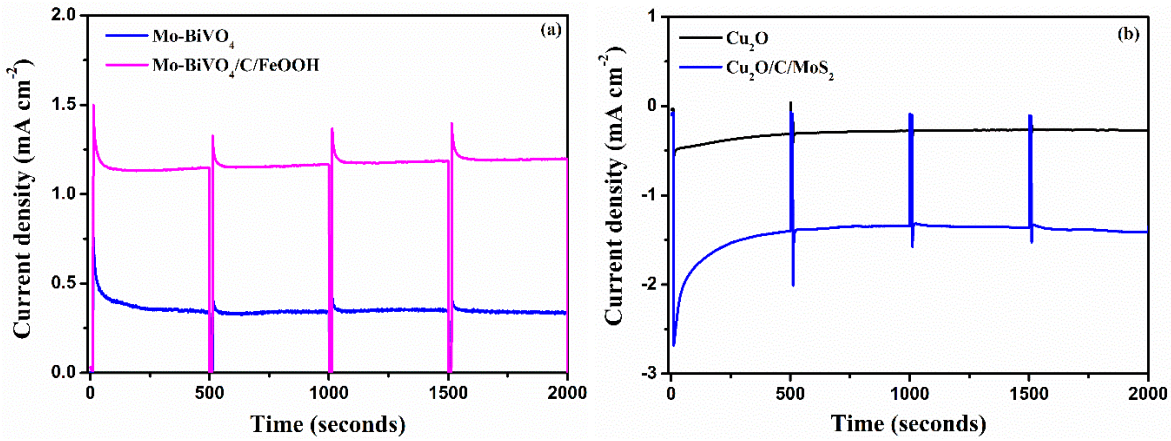

Figure S8, *Chronoamperometry (J vs. t) stability tests of (a) Mo-$BiVO_4$, Mo-$BiVO_4$/C/FeOOH photoanodes performed at 1.23 V vs RHE, (b) Cu_2O, Cu_2O/C/MoS_2 photocathodes performed at 0 V vs RHE using 0.1 M Na_2SO_4 (pH 6) electrolyte in AM 1.5 G illumination with power intensity of 100 mW cm^{-2}*

The stability tests of photoanodes were performed at the water oxidation potential (1.23 V vs. RHE) and the stability tests of photocathodes were performed at water reduction potential (0 V vs. RHE) by chopping the illumination off for every 500 seconds. Figure S8 (a) shows the J vs. t curves of photoanodes for which Mo-$BiVO_4$ attained a current density of 0.75 mA cm^{-2} and the current steadily decreased to 0.35 mA cm^{-2} in the end of the testing window. On the other hand, the Mo-$BiVO_4$/C/FeOOH photoanode attained a maximum current density of 1.48 mA cm^{-2} when illuminated and remained at current density of 1.14 mA cm^{-2} throughout the testing time of 2000 seconds. The current density obtained was equivalent to the current density at water oxidation potential in the LSV curves (figure 4 (a) in manuscript). The stability tests of bare Cu_2O was unstable due the photocorrosion. Current density of -0.27 mA cm^{-2} was obtained for Cu_2O photocathodes which decreased at the end of the stability test. For Cu_2O/C/MoS_2 photocathode, the obtained current density was -1.43 mA cm^{-2} (at 400 seconds) and it sustained the current density till the end of the testing time. The current density at the end of the Cu_2O/C/MoS_2 photocathode was -1.41 mA cm^{-2}. The improvement in current density and the stability of the photoelectrodes are due to the addition of co-catalyst and the carbon protective layer.

2.2 *Estimation of efficiencies of $BiVO_4$ photoanodes using hole scavenger*

To investigate the material performance of the photoanode in terms of efficiencies, linear sweep voltammetry (LSV) measurements are performed using hole scavengers. The photoelectrochemical process is shown in equation as,

$$J_{PEC} = J_{abs} \times \eta_{separation} \times \eta_{injection} \quad (1)$$

Here J_{PEC} is the measured photocurrent density obtained from the LSV analysis, J_{abs} is the photon absorption rate obtained from the UV-vis absorption spectrum of photoanode. $\eta_{separation}$ is the charge separation efficiency, which is the measure of photogenerated carriers that reaches

the surface of the photoanode. $\eta_{injection}$ is the charge injection efficiency which is the measure of surface reaching minority carriers that are injected into the electrolyte solution.

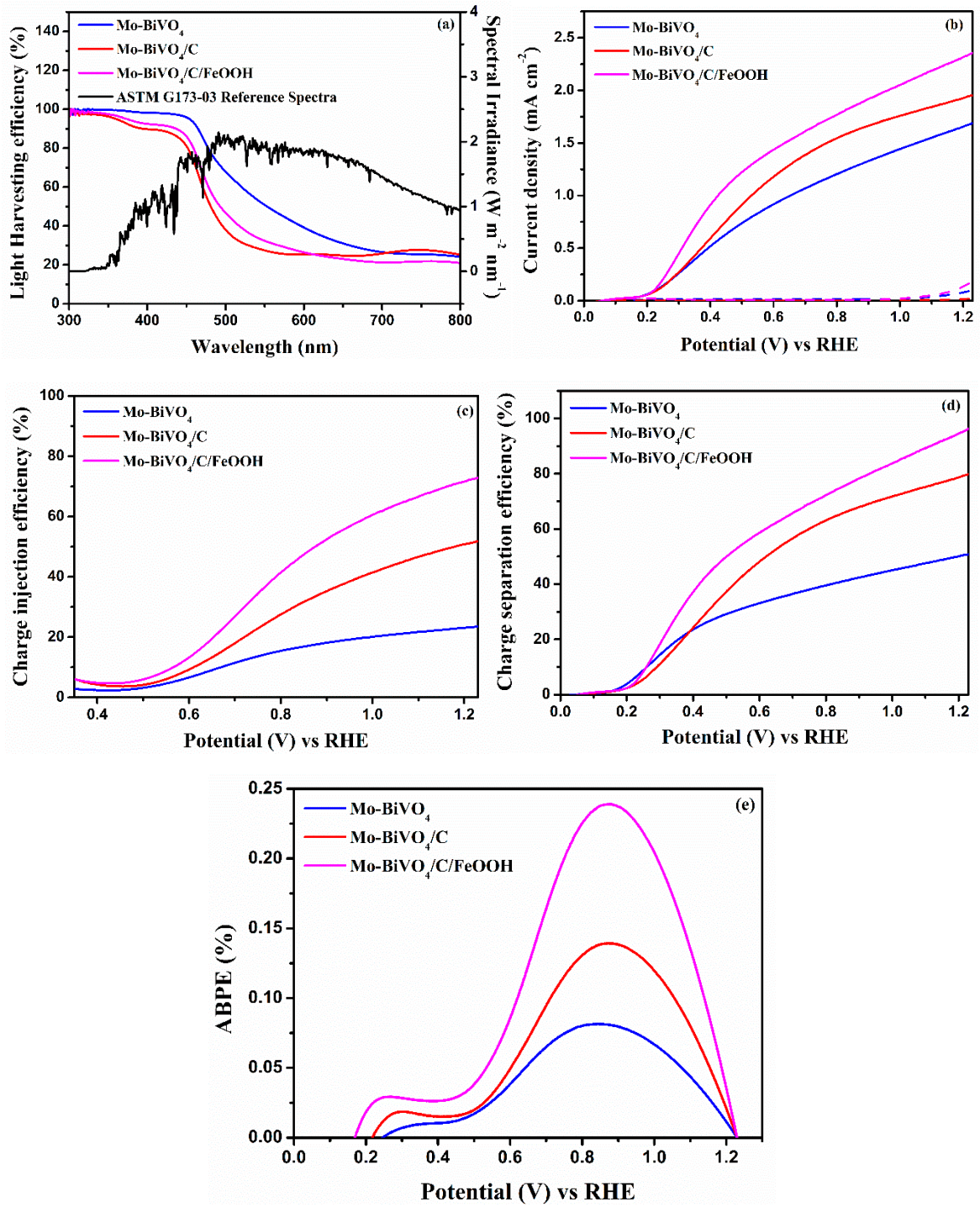

Figure S9, *(a) Light harvesting efficiency with respect to standard solar spectrum, (b) LSV curves using 0.1 M Na_2SO_3 + 0.1 M Na_2SO_4 (pH 6) electrolyte, (c) Charge injection efficiency, (d) Charge separation efficiency and (e) Applied bias photon-to-current efficiency of Mo-$BiVO_4$, Mo-$BiVO_4$/C and Mo-$BiVO_4$/C/FeOOH photoanodes*

$$\text{Charge separation efficiency, } \eta_{separation} = \frac{J_{Na2SO3}}{J_{max}} \qquad (2)$$

Charge injection efficiency, $\eta_{injection} = = \frac{J_{H2O}}{J_{Na2SO3}}$ (3)

Applied bias Photon-to-current efficiency, $ABPE = \frac{J \times (1.23 - V_b) \times \eta_f}{P_{total}}$ (4)

Figure S9 (a) shows the light harvesting efficiency of $BiVO_4$ photoanodes with respect to the standard solar spectrum. It was observed that the photons are absorbed by the photoanodes up to ~95% within the absorption edge. Figure S9(b) shows the linear sweep voltammetry (LSV) curves of $BiVO_4$ photoanodes tested in 0.1 M Na_2SO_3 + 0.1 M Na_2SO_4 (pH 6) electrolyte. Figure S9 (c) shows the charge separation efficiency of $BiVO_4$ photoanodes. The maximum charge separation efficiency of 96.4 % was obtained for Mo-$BiVO_4$/C/FeOOH photoanode at 1.23 V vs RHE. There was two-fold increase in the charge separation efficiency due to the addition of carbon layer and FeOOH co-catalyst. Figure S9 (d) shows the charge injection efficiency of $BiVO_4$ photoanodes. The charge injection efficiency was 72.6 % for Mo-$BiVO_4$/C/FeOOH photoanode at 1.23 V vs RHE, which was three-fold increase than the Mo-$BiVO_4$ photoanode. The result indicates that synergic effects of carbon layer and co-catalyst layers aids in improving the slow water oxidation kinetics. Carbon layer acts as a window layer in transporting the photogenerated holes to the surface of the photoanode. The significant improvement in charge separation efficiency is due to the addition of carbon layer. Figure S9 (e) shows the Applied bias photon-to-current efficiency (ABPE) of $BiVO_4$ photoanodes. ABPE was measured in 0.1 M Na_2SO_4 (pH 6) electrolyte and the maximum ABPE of 0.23% was observed for Mo-$BiVO_4$/C/FeOOH photoanode.

2.3 Equivalent circuit from Electrochemical Impedance spectroscopy (EIS)

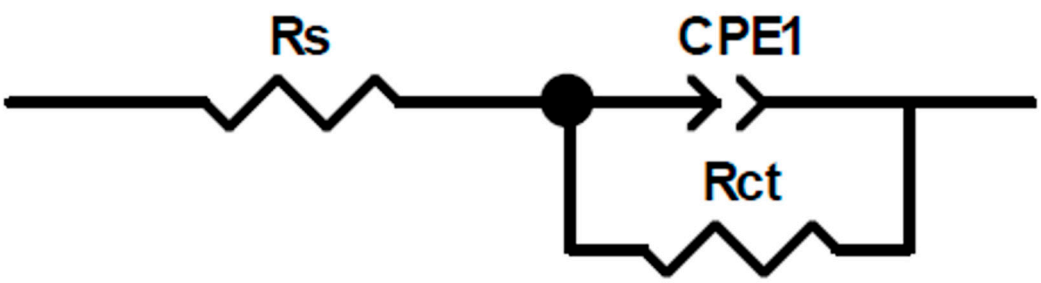

Figure S10, *EIS equivalent circuit of $BiVO_4$ photoanodes and Cu_2O photocathodes*

2.4 Mott-Schottky analysis

In order to gain insight about the band structure and carrier concentration of the photoanode/ photocathode, Mott Schottky plots were recorded. The Mott-Schottky plot is the plot between the inverse of square of space charge capacitance (C_{sc}) to the potential vs RHE. The Mott-schottky equation was,

$$\frac{1}{C_{sc}^2} = \frac{2}{\varepsilon_r \varepsilon_0 A^2 e N_{Dopant}} \left(E - E_{fb} - \frac{kT}{e}\right) \quad (5)$$

Mott-Schottky plot (figure S11 a to c) was recorded for the photoanode in dark condition at 1 kHz frequency. The positive slope expresses that photoanode is an n-type semiconductor. Mott-Schottky plots are used to calculate flat band potential and the donor concentration of the

semiconductor [37]. The flat band potential E_{FB} can be found by extrapolating an intercept in the x-axis [38]. The E_{FB} value of Mo-$BiVO_4$ was estimated to be 0.025 V vs RHE. The Mo-$BiVO_4$/C/FeOOH photoanode exhibited the flat band potential of -0.171 V vs RHE. This is because of the synergic effect of carbon layer and FeOOH catalyst layer which improves the slow water oxidation kinetics by reducing the overpotential of water oxidation. Charge Carrier concentration can be calculated by slope of the obtained Mott-Schottky curve [39]. The carrier concentration of Mo-$BiVO_4$ and Mo-$BiVO_4$/C was 4.70×10^{19} cm^{-3} and 5.68×10^{20} cm^{-3}, respectively. The Mo dopant and addition of carbon layer increases the donor concentration. Similarly, the negative slope of the Mott-Schottky plot of photocathode (figure S11 d to f) proves the p-type behaviour of photocathode semiconductor. The E_{FB} of the Cu_2O photocathode was 0.595 V vs RHE. The flat band potential was anodically shifted to 0.606 V vs RHE for Cu_2O/C photocathode. Cu_2O/C/MoS_2 photocathode produced positive flat band potential of 0.74 V vs RHE. The increase in the E_{FB} provides higher band bending and large space charge region potential. The higher space charge region potential is due to the deposition of carbon layer. Tabulation of flat band potential and Dopant concentration is tabulated in table 1.

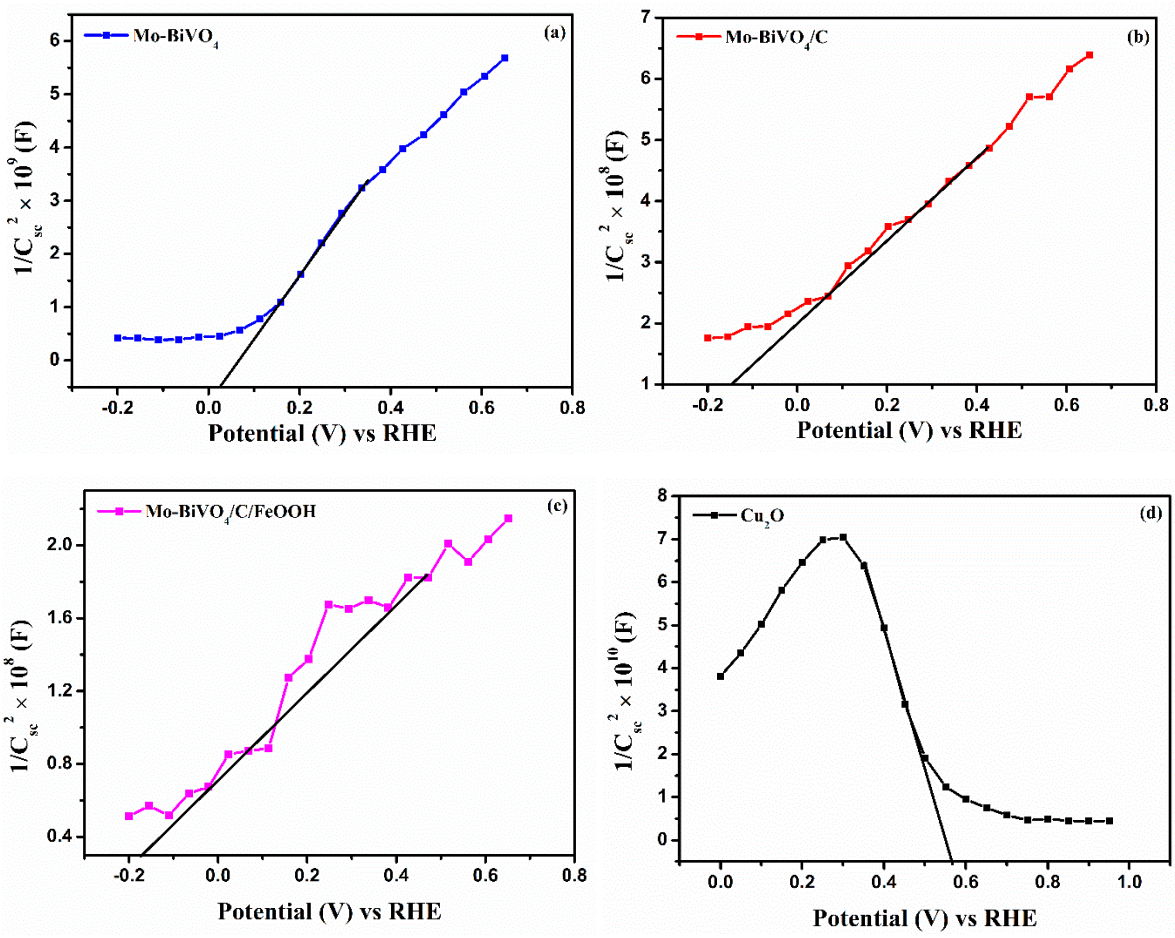

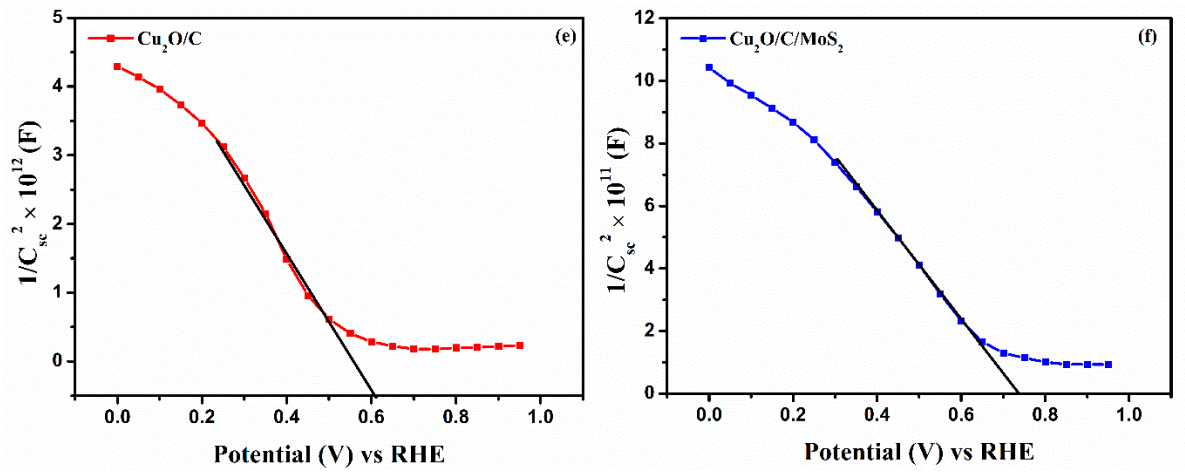

Figure S11, *Mott-Schottky plot of (a) Mo-$BiVO_4$, (b) Mo-$BiVO_4$/C and (c) Mo-$BiVO_4$/C/FeOOH photoanodes, (d) Cu_2O and (e) Cu_2O/C and (f) Cu_2O/C/MoS_2 photocathodes tested in dark condition at 1 kHz frequency in 0.1 M Na_2SO_4 (pH 6)*

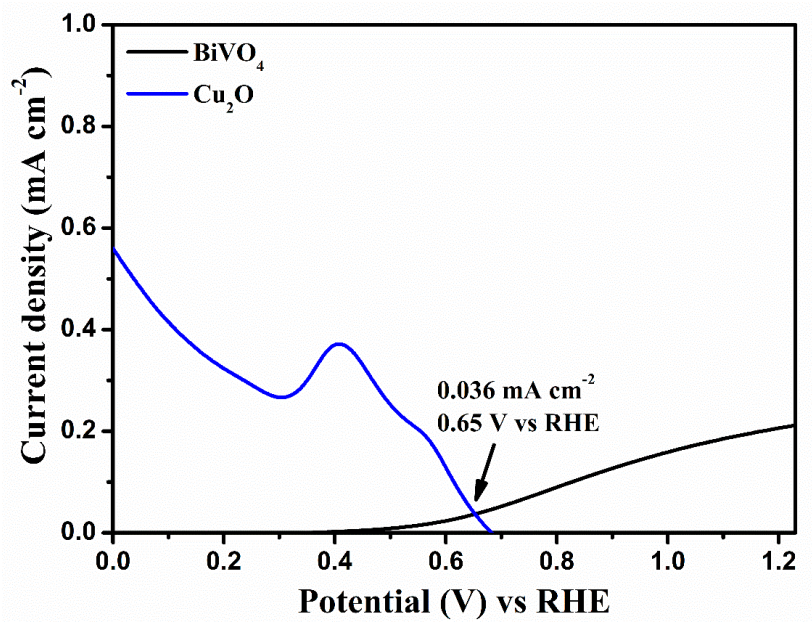

Figure S12, *Overlayer LSV curves of $BiVO_4$ photoanodes and Cu_2O photocathodes tested in 0.1 M Na_2SO_4 (pH 6) using AM 1.5 G light source with power intensity of 100 mW cm^{-2}*

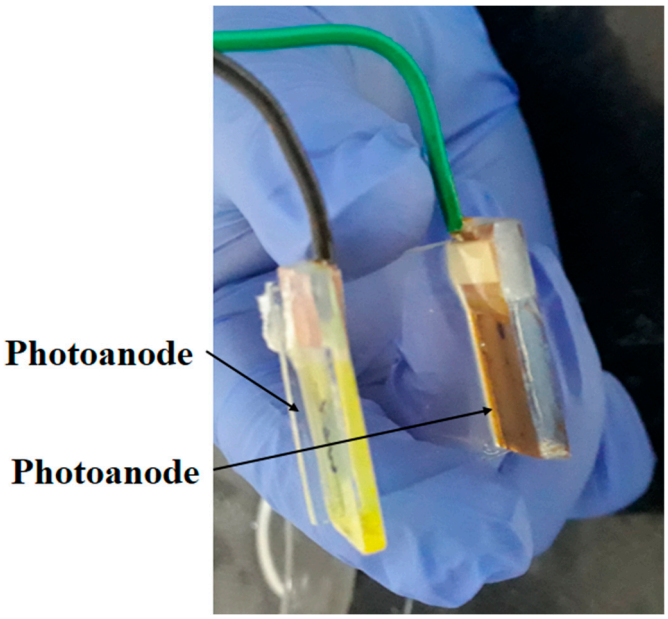

Figure S13, *Photographs of of Mo-$BiVO_4$/C/FeOOH-Cu_2O/C/Mos_2 tandem cell*

Table S3, *Comparison of Mo-$BiVO_4$/C/FeOOH photoanode and Cu_2O/C/MoS_2 photocathode with works performed using carbon based materials*

Photoanode	Method of deposition of Carbon material	Electrolyte (pH)	Current density at 1.23 V vs RHE	Ref.
$BiVO_4$/CNT	Carbon Nanotubes (CNT) mixed with precursor and spin coating method	0.1 M K_2HPO_4 (pH 8)	1.2 mA cm^{-2}	[11]
CNT/$BiVO_4$	BiVO4 coated on top of CNT	0.5 M KPi buffer (pH 6.8)	0.4 mA cm^{-2}	[40]
$BiVO_4$/CQD/FeOOH/ NiOOH	Carbon quantum dots (CQD) deposited by ageing	Potassium phosphate buffer (pH 7)	5.99 mA cm^{-2}	[41]
$BiVO_4$/Carbon spheres	Carbon spheres are coated on BiVO4 by spin coating method	KPi buffer (pH 7)	2.5 mA cm^{-2}	[42]
$BiVO_4$/rGO	Reduced graphene oxide (rGO) was coated by spin coating method	0.5 M Na_2SO_4 (pH 6.9)	0.75 mA cm^{-2}	[12]
$BiVO_4$/NSCN/CoPi	N,S co-doped carbon nanosheets were deposited by thermal decomposition of dithiooxamide	0.1M potassium phosphate buffer (pH 7)	3.2 mA cm^{-2}	[14]
Mo-$BiVO_4$/C/FeOOH	Carbon layer was deposition by thermal	0.1M Na_2SO_4	1.22 mA cm^{-2}	THIS WORK

	decomposition of glucose	(pH 6)		
Photocathode	**Method of deposition of Carbon material**	**Electrolyte (pH)**	**Current density at 0 V vs RHE**	**Ref.**
$Cu_2O/CuO/C$	Carbon layer was deposited by thermal decomposition of glucose	1M Na_2SO_4	-7 mA cm^{-2}	[15]
Carbon coated Cu_2O nanoneedles	Carbon layer was deposited by thermal decomposition of dextrose	0.1M phosphate buffer (pH 5)	-0.4 mA cm^{-2}	[16]
Carbon coated Cu_2O nanowire	Carbon layer was deposited by thermal decomposition of glucose	0.5M Na_2SO_4 (pH 6.23)	-2.7 mA cm^{-2}	[43]
$ZnO/Cu_2O/rGO$	rGO was deposition by cathodic electrodeposition	0.5M Na_2SO_4	-10.11mA cm^{-2}	[44]
$Cu_2O/Ti_3C_2T_x$	Mxene was deposited by immersing Cu2O in Mxene solution and annealing at Ar atmosphere	1M Na_2SO_4 (pH 5)	-4.45 mA cm^{-2}	[45]
$Cu_2O/C/MoS_2$	Carbon layer was deposition by thermal decomposition of glucose	0.1M Na_2SO_4 (pH 6)	-1.48 mA cm^{-2}	THIS WORK